High heat flow from Enceladus' south polar region measured using 10–600 cm^{-1} Cassini/CIRS data

C. J. A. Howett,[1] J. R. Spencer,[1] J. Pearl,[2] and M. Segura[2]

Received 24 August 2010; revised 9 November 2010; accepted 21 December 2010; published 4 March 2011.

[1] Analysis of 2008 Cassini Composite Infrared Spectrometer (CIRS) 10 to 600 cm^{-1} thermal emission spectra of Encleadus shows that for reasonable assumptions about the spatial distribution of the emission and the thermophysical properties of the solar-heated background surface, which are supported by CIRS observations of background temperatures at the edge of the active region, the endogenic power of Enceladus' south polar terrain is 15.8 ± 3.1 GW. This is significantly higher than the previous estimate of 5.8 ± 1.9 GW. The new value represents an improvement over the previous one, which was derived from higher wave number data (600 to 1100 cm^{-1}) and was thus only sensitive to high-temperature emission. The mechanism capable of producing such a high endogenic power remains a mystery and challenges the current models of proposed heat production.

Citation: Howett, C. J. A., J. R. Spencer, J. Pearl, and M. Segura (2011), High heat flow from Enceladus' south polar region measured using 10–600 cm^{-1} Cassini/CIRS data, *J. Geophys. Res.*, *116*, E03003, doi:10.1029/2010JE003718.

1. Introduction

[2] In July 2005, instruments on board the Cassini spacecraft detected endogenic heat and plume activity at Enceladus' south pole associated with four prominent fractures (sulci) commonly referred to as tiger stripes [*Spencer et al.*, 2006; *Hansen et al.*, 2006; *Porco et al.*, 2006; *Spahn*, 2006]. Triangulation of Imaging Science Subsystem (ISS) images shows that these sulci are also the sources of the observed plumes [*Spitale and Porco*, 2007]. Initial analysis of midinfrared data (600 to 1100 cm^{-1}) taken by focal plane 3 (FP3) of the Composite Infrared Spectrometer (CIRS) onboard Cassini indicated that the endogenic power of Enceladus' south polar region was 5.8 ± 1.9 GW [*Spencer et al.*, 2006], much higher than the expected radiogenically produced power of 0.3 GW [*Porco et al.*, 2006; *Schubert et al.*, 2007]. Dissipation of tidally produced energy, most likely from the Dione and Enceladus 2:1 resonance, has been suggested as a possible production mechanism of the observed endogenic power [*Spencer et al.*, 2006; *Porco et al.*, 2006; *Yoder*, 1979; *Ross and Schubert*, 1989].

[3] It has been shown that over the long term this and other resonances are unable to produce an endogenic power greater than 1.1 GW if the dissipation factor Q of Saturn is frequency-independent [*Meyer and Wisdom*, 2007]. However, higher sustainable endogenic powers could be produced if the Q of Saturn that applies to Enceladus is lower than the value of 18000 used by Meyer and Wisdom, which was determined by limits on the change of Mimas' semi-major axis over 4.6 Gy. If Saturn's Q today is different from the time-averaged value, or if the Q that applies to Enceladus' orbital frequency is different from the one applicable to Mimas' orbital frequency, then higher heat flows from Enceladus could be sustainable [*Lainey et al.*, 2010; *Meyer and Wisdom*, 2010].

[4] Greater tidal heating would also be predicted if Enceladus' silicate interior and outer ice shell were decoupled by a global subsurface ocean or localized subsurface south polar sea [*Collins and Goodman*, 2007; *Nimmo et al.*, 2007; *Tobie et al.*, 2008; *Roberts and Nimmo*, 2008], though the long-term steady state upper limit discussed above still applies. Liquid water has been suggested to exist close to the surface, at the plume source [*Spencer et al.*, 2006; *Porco et al.*, 2006]. This argument was recently strengthened by the discovery of salt-rich particles [*Postberg et al.*, 2009] and ammonia and ^{40}Ar in the plume [*Waite et al.*, 2009]. Never the less the possibility of liquid water, a tidal energy source and the observation of organics on the surface of Enceladus [*Brown et al.*, 2006] make the satellite a site of strong astrobiological interest.

[5] The *Spencer et al.* [2006] calculation of Enceladus' endogenic power found that blackbody emission at 133 ± 12 K over an area of 345^{+320}_{-160} km^2 matched the total >600 cm^{-1} CIRS FP3 spectrum of the south polar region. However, at this temperature only 10% of the blackbody spectral energy falls within the FP3 wave number range, while the remaining 90% of it falls within the 10 to 600 cm^{-1} wave number range of CIRS' focal plane 1 (FP1). The percentage of the spectral energy in the FP3 wave number range decreases further with decreasing temperature, rendering FP3 insensitive to low-temperature emission, and it was noted by *Spencer et al.* [2006] that additional power might be radiated at lower temperatures.

[1]Southwest Research Institute, Boulder, Colorado, USA.
[2]NASA Goddard Space Flight Center, Greenbelt, Maryland, USA.

Copyright 2011 by the American Geophysical Union.
0148-0227/11/2010JE003718

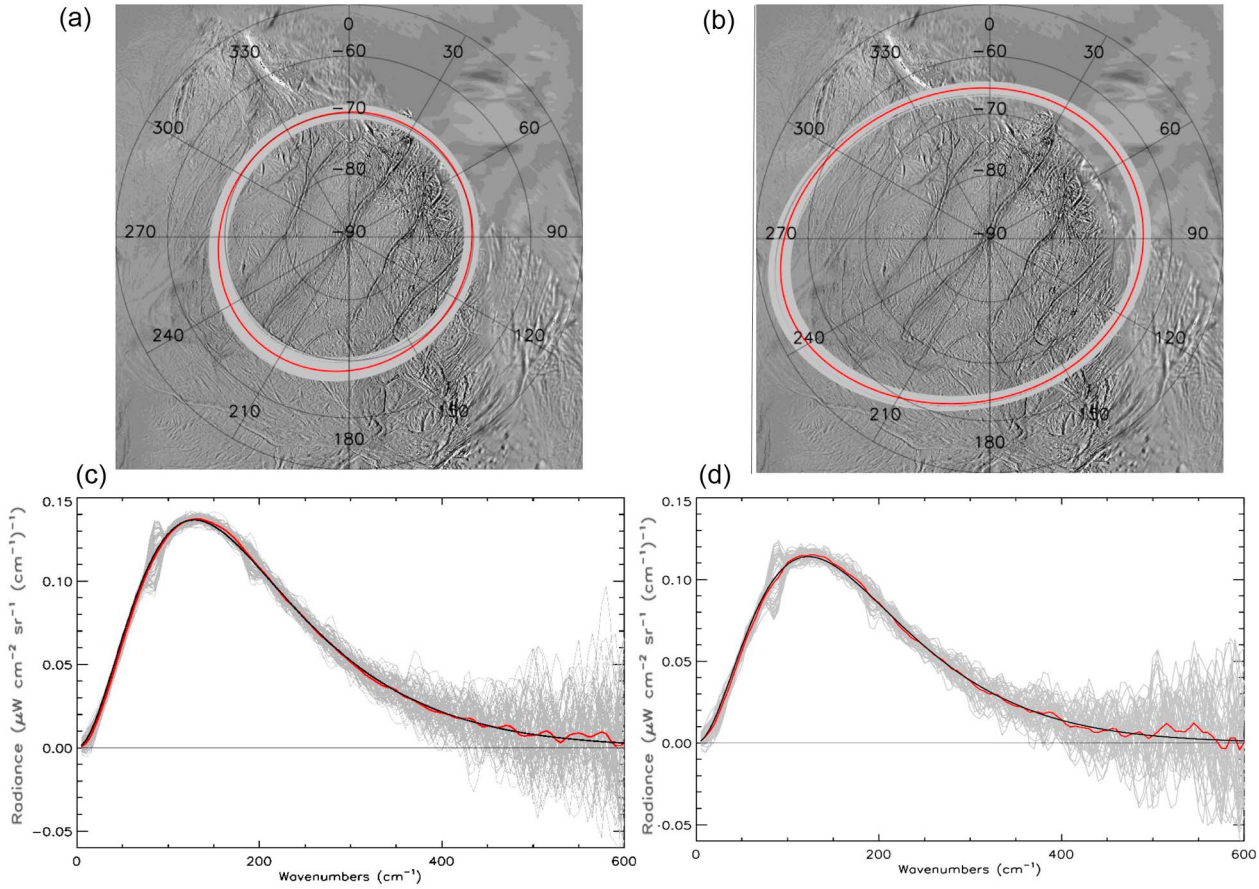

Figure 1. (a and b) The range of locations of the FP1 field of view during the stare observations of rev 61 (Figure 1a) and rev 91 (Figure 1b) over Enceladus' south pole (shown in gray). The field of view at the observation midtime is also shown (red). The four prominent fractures within the rev 61 field of view are the active tiger stripes. The base map used is the 2006 ISS mosaic PIA 08342. (c and d) The spectra of each stare observation (gray), the mean spectrum (red), and the best fit two-temperature to this mean value (black) for revs 61 (Figure 1c) and 91 (Figure 1d).

[6] CIRS is a Fourier Transform Spectrometer consisting of two interferometers, which share a scan mechanism and telescope [*Flasar et al.*, 2004]. The midinfrared is detected by a Michelson interferometer and two linear focal plane arrays of 10 HgCdTe detectors which each have a 0.273 mrad field of view. These focal planes, known as FP3 and FP4, measure from 600 to 1100 cm^{-1} and from 1100 to 1400 cm^{-1}, respectively. FP1 is a polarizing interferometer with two thermopile detectors that cover the far infrared (10–600 cm^{-1}) and are thus sensitive to lower temperatures than FP3 or FP4. The FP1 detectors have a single circular field of view with a nonuniform spatial response, the effect of which is discussed in section 2.2.

[7] High-quality FP1 spectra, whose wave number range captures the majority of the radiated power from both the warmer active and cooler inactive regions of Enceladus, have recently been obtained for Enceladus' south polar terrain. The data have a spectral resolution of 15 cm^{-1} and a spatial resolution that varies from 800 m near closest approach to complete hemispherical coverage. Long integrations (known as stares) were targeted at Enceladus' south polar region on 12 March 2008 (orbit, or revolution (hereafter rev), 61) and 31 October 2008 (rev 91). The signal to noise of each data set is increased by averaging the stares together. These stares are the only FP1 observations that will be made over the entire Cassini mission which both cover the entire south polar terrain and are sensitive to the wave number region where the bulk of the endogenic power is radiated. Figure 1 shows the stare locations: each of the 73 integrations in rev 61 and the 48 integrations in rev 91 has comparable geometry. In addition to these stares scattered high spatial resolution FP1 observations of the region were obtained on those dates and on 11 August 2008 (rev 80).

[8] Figure 1 also shows the calibrated spectra of these observations, along with the average spectrum and the best fit combination of two blackbodies, with both the temperatures of the two blackbodies and their relative fractional coverage of the CIRS field of view being fitted as free parameters. The rev 61 data are fitted using 90.9 K over 14% of the average 26,619 km^2 field of view, with the remainder of the area at 56.0 K. The rev 91 data are best fitted by blackbody emission at 80.7 K over 22% of the average 47,199 km^2 field of view, with the remainder of the area at 50.4 K. Thus, the total power observed in the mean

spectra for the rev 61 and 91 stares, using the Stefan-Boltzmann law, is 27.3 GW and 38.2 GW. If the endogenic emission is assumed to be the high-temperature component of these fits then the endogenic power is 14.6 GW and 24.8 K. However, this assumption does not fully account for any low-temperature endogenic emission, which could be only a little warmer than that of the passive (i.e., reradiated sunlight) emission [*Abramov and Spencer*, 2009], or the fact that the passive temperatures will also vary across the CIRS field of view. Thus a more sophisticated approach is needed to determine the endogenic emission that makes no assumptions about the temperature distribution of the emission.

2. Calculating the Endogenic Emission

2.1. Introduction

[9] FP1 is sensitive to the passive emission from the solar-heated surface, which has temperatures in the 35–80 K range [*Spencer et al.*, 2006]. Thus, to obtain the endogenic component of the spectra this passive emission must first be removed. Passive emission is modeled for each epoch and observational geometry using a seasonal and diurnal 1-D numerical thermal model [*Spencer et al.*, 1989]. The model determines surface temperatures by calculating conductive heat flow into and out of the subsurface through every diurnal cycle of an entire Saturnian year, accounting for insolation variations resulting from the 29° tilt of Enceladus' rotation axis relative to the sun, and the concurrent changes in heliocentric distance (from 9.03 to 10.05 AU) resulting from Saturn's orbital eccentricity. The model assumes that albedo does not vary with incidence angle, and does not initially account for the effects of heating by radiation from Saturn, or solar eclipses by Saturn, though these are discussed in section 2.3. The thermal inertia values it uses are based on previous observations but require assumptions about the thermophysical properties at depth. The extent to which these assumptions affect our estimate of the endogenic power from Enceladus are discussed further in sections 2.3 to 2.6.

[10] For each observation the temperatures predicted by this model are used to calculate the passive background across the FP1 field of view, assuming blackbody emission. These temperatures are weighted by the spatial sensitivity pattern of the FP1 detector, which is approximated as a 2-D Gaussian with a FWHM of 2.42 mrads [*Flasar et al.*, 2004]. The results from this model are validated in section 2.6 by demonstrating the good agreement between the modeled spectrum produced, and CIRS data taken within Enceladus' south polar terrain but away from the tiger stripes themselves.

[11] For each observation this passive thermal background is subtracted from the CIRS spectra leaving a residual, the spectrum of the endogenic emission. The residual is then weighted to correct for the assumed spatial distribution of the endogenic emissions. Three possible scenarios are considered: that emission from the tiger stripes is uniform along their length, that the emission from the stripes varies in the same way as previously observed by higher spatial resolution higher wave number observations by the CIRS FP3 detector and, to set a lower limit on the endogenic power, a scenario which all emission arises from the most sensitive central 10% of the field of view is also considered. The effects these scenarios have on the endogenic emission determination are discussed further in section 2.2. In the case of the stare observation the corrected residuals for each rev are averaged to increase the signal to noise. The final corrected residual is then fitted by a blackbody temperature curve with a filling factor, which allows the residual to be fitted by emission from only a fraction of the field of view if required. The endogenic power of that residual is then derived using the Stefan-Boltzmann law, the fitted temperature, filling factor and area of the projected FP1 field of view.

2.2. Characterizing the Uncertainties of the Spatial Response of the FP1 Detector and the Spatial Distribution of the Endogenic Power

[12] The total endogenic power determined depends on both the spatial distribution of the endogenic emission and that of the FP1 detector sensitivity. The spatial response of the FP1 detector is assumed to be a Gaussian with a FWHM of 2.51 mrads [*Smith*, 2002]. The actual FP1 spatial response observed in flight however is flatter at the center than a Gaussian. The FWHM of the observed response is 2.42 mrads, indicating that the response drops off more quickly than the previously assumed value. The normalized response drops to a value of 0.01 at a diameter of 6.2 mrads, which is much wider than the commonly cited field of view of 3.9 mrads [*Flasar et al.*, 2004]. Both of these FWHM values are much lower than the FWHM of 2.71 mrads determined for FP1 during ground testing [*Smith*, 2002]. However, as Figure 2 shows for a constant bolometric Bond albedo value of 0.80 and thermal inertia scenario 2 the effect of varying the FWHM of the FP1 response function from 2.42 to 2.51 (the values observed and routinely used since launch) over a diameter of 3.9 to 6.2 mrads is small (<1.2 GW). For the remainder of this work the response of the FP1 detector is assumed to be Gaussian with a FWHM of 2.42 mrads and response is integrated out to a diameter of 3.9 mrads.

[13] Since the response of the FP1 detector is nonuniform it is sensitive to the spatial distribution of the endogenic emission. To estimate the dependence of the derived endogenic emission on its spatial distribution we evaluate three different scenarios: that the tiger stripes are the sole source of the power and have uniform emission along their lengths; that the tiger stripes are the sole source of the power but that the emission intensity varies along each stripe; and finally that the emission is independent of the tiger stripes location but arises instead from an area within the most sensitive central 10% of the FP1 field of view. The last scenario is unrealistic but is designed to determine a lower limit to the endogenic emission. The FP1 detector is most sensitive to emission from its central region and thus concentration of the emission in this region would minimize the true power required to produce the observed signal.

[14] Under the second scenario the variation in brightness along the length of the tiger stripes is assumed to be the same as that determined from high spatial resolution 600–1100 cm^{-1} FP3 observations made on rev 61 (Figure 3 and Table 1) from 1922:00 to 1944:00 UT. These observations had a spatial resolution of 4.1–9.6 km, sufficient to resolve the tiger stripes and the spatial distribution of emission along their lengths (Figure 3 and Table 1). Almost the entire tiger stripe region was covered, with the exception of the Saturn-facing end of Alexandria Sulcus, for which we have

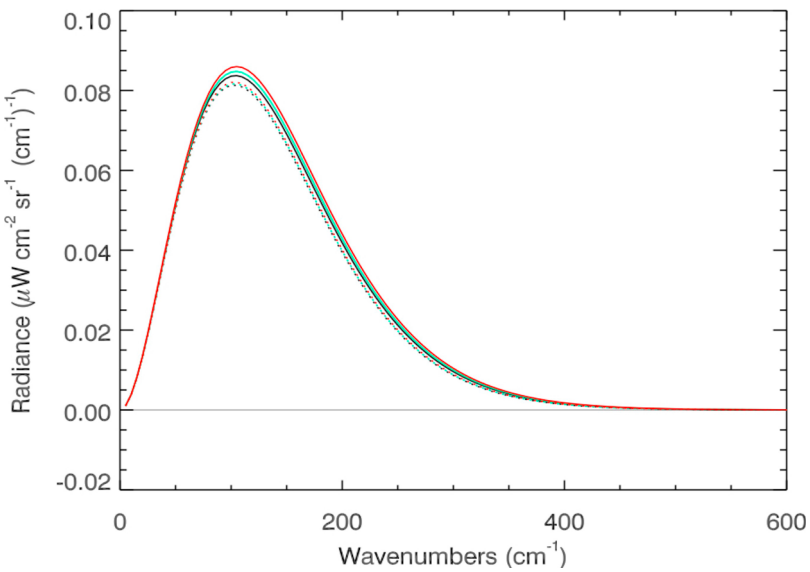

Figure 2. The effect that varying the response of the FP1 detector and the modeled spatial distribution of the endogenic emission has on the predicted passive emission for the central stare observation in the rev 91 data set (31 October 2008 at 1807:45 UT). The temperatures were calculated using the technique outlined in section 2.1 using a constant bolometric Bond albedo of 0.80, thermal inertia scenario 2, and a number of assumed FWHM values and maximum diameters for the spatial response of the FP1 detector. The black, blue, and red lines show the modeled passive emission when the FP1 spatial response is assumed to a Gaussian with a FWHM of 2.40, 2.51, and 2.70, respectively. The solid and dotted lines indicate that diameters of 6.2 mrad and 3.9 mrad (the nominal value), respectively, are assumed for the outer boundary of the response of the FP1 detector.

included approximate brightness values based on other CIRS observations [*Spencer et al.*, 2006]. For the "uniform" case, we assigned equal brightness to all spatial bins with nonzero normalized brightness in Table 1.

[15] The assumed spatial variation in the endogenic emission has a much larger effect on the derived total endogenic power than the plausible variations in the FP1 spatial response. We quantify this effect as the ratio between the derived power P and the power P_U derived by assuming that the endogenic emission uniformly fills the nominal 3.9 mrad FP1 field of view. As expected, the scenario with the emission concentrated in the center of the field of view results in the smallest derived power: $P/P_U = 0.6$ for both rev 61 and rev 91 data. For the other two scenarios $P/P_U =$ 1.1 and 0.9 for the rev 61 and rev 91 observations if uniform emission is assumed, and $P/P_U = 0.9$ and 0.8 for the revs 61 and 91 observations, respectively, if the FP3-like nonuniform emission is assumed. These corrections resulted in variations of up to 3.3 GW in the endogenic emission predicted for the uniform emission and FP3-like spatial emission distributions depending on the thermophysical properties assumed, as discussed further below.

2.3. Solar Eclipses by Saturn and Saturn Heating

[16] The side of Enceladus that faces Saturn (longitude >270°W and <90°W) is heated not just by the sun, but by Saturn, which has an effective temperature of 95.0 K [*Hanel et al.*, 1983]. Enceladus' albedo in the thermal infrared is very low, as inferred from the near-blackbody nature of its thermal emission, which implies high emissivity. Enceladus therefore absorbs almost all the incident Saturn radiation, increasing the importance of this heat source relative to sunlight, 80% of which is reflected due to Enceladus' high visible wavelength albedo. There is a very small additional component of heating due to reflected sunlight from Saturn: due to Saturn's relatively low geometric albedo of 0.23 [*Hanel et al.*, 1983], and Enceladus' high visible albedo, adding this component is equivalent to increasing the diurnally averaged effective temperature of Saturn to 95.8 K. Counteracting heating from Saturn, the Saturn-facing side of Enceladus also experiences an interruption of sunlight every day for up to several hours during much of the year, due to solar eclipses by Saturn. This interruption results in the cooling of the surface, which if not corrected for would result in the passive emission being overestimated, thus underestimating the endogenic emission.

[17] We have constructed thermal models that include both these Saturn-related effects. Because temperatures then depend on longitude as well as latitude and local time, computation times are greatly increased, so we have computed temperatures for only one set of thermophysical parameters, the case with a vertically homogeneous thermal inertia of 27 J m^{-2} K^{-1} $s^{-1/2}$ (the units of which are henceforth referred to as MKS) (scenario 1 and Table 3). This model shows that the heating effect of Saturn is greater than the cooling effect of the eclipses for most of the year, so that the Saturn-facing side of Enceladus is slightly warmer, for constant thermophysical properties, than the anti-Saturn hemisphere. Near equinox, including the time of the south polar observations reported here, when Saturn eclipses have close to maximum duration, diurnally averaged temperatures on the two hemispheres are very similar,

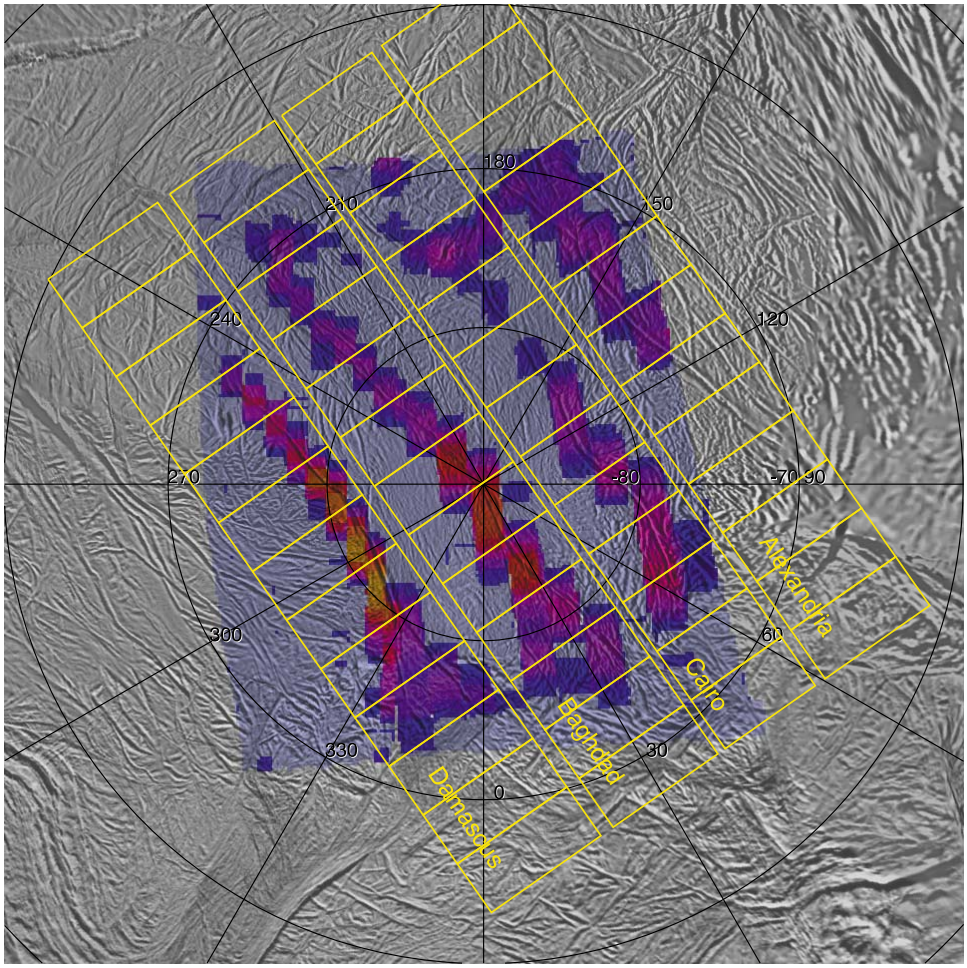

Figure 3. CIRS FP3 map of the spatial distribution of radiated 600–1100 cm^{-1} brightness along the four tiger stripes, as observed on 12 March 2008 (rev 61). Relative brightness is shown by colors ranging from blue (faintest) to yellow (brightest). The pale blue area shows regions that were mapped but showed negligible radiated power. The yellow rectangles indicate the spatial bins within which the power values listed in Table 1 were summed. The data used in this scan was taken between 1922:00 and 1944:00 UT on the 12 March 2008.

though temperatures on the Saturn-facing side drop during the eclipses themselves (Figure 4a).

[18] The highest spatial resolution CIRS observations of Enceladus' south pole made during revs 80 and 91 were taken in sunlight. However, the stare observations from these revs, and all south polar observations obtained during rev 61, were taken when Enceladus was in eclipse by Saturn. Because passive background temperatures cool during the eclipse, passive models that do not account for the eclipse will overestimate the passive contribution to the signal, and thus underestimate the endogenic contribution. In rev 61, the eclipse covered the time period 1905:13–2118:06 UT and the FP1 stare observations covered the period 1955:29–2001:20 UT: the observation midpoint was thus 53 min after eclipse ingress. In rev 91, the eclipse covered 1804:26–2036:56 UT and the observations covered 1805:48–1809:46 UT, so the observation midpoint was just 3 min after eclipse ingress and it is expected that these observations will be less affected by the eclipse than the rev 61 data.

[19] An example of the cooling effect of an eclipse at one location on the surface, at 80°S, 0°W during rev 91, is shown in Figure 4a. This location was selected as it represents longitudes most affected by eclipses, i.e., those that experience eclipses during times at which the solar insolation would otherwise be at its maximum. Figure 4a shows that under this worst case scenario at 80°S, a longitude that surrounds the SPT, ignoring eclipses results in the passive thermal background being overestimated by less than 2 K. Similar curves are observed for the bolometric Bond albedo values shown in Figure 4b.

[20] We tested the sensitivity of surface temperature to the combined effect of Saturn shine and eclipses for both the rev 61 and 91 stare observations for thermophysical property scenario 1 (see section 2.4). The results are shown in Figure 5, which shows that the surface temperatures along the midday and midnight meridian, assuming a constant bolometric Bond albedo of 0.80 and thermal inertia profile of 27 MKS, are not significantly affected at this epoch by these effects (<2 K). By subtracting the passive thermal backgrounds predicted by the model when Saturn shine and eclipse events are included and ignored from the CIRS spectrum, applying the spatial distribution correction

Table 1. Relative 600–1100 cm^{-1} Brightness of the Tiger Stripes, in Spatial Bins at the Specified Locations Along the Length of the Four Tiger Stripes, Observed by the CIRS FP3 Detector on 12 March 2008, Rev 61[a]

Center		Corner 1		Corner 2		Corner 3		Corner 4		Normalized	
Latitude	Longitude	Latitude	Longitude	Latitude	Longitude	Latitude	Longitude	Latitude	Longitude	Brightness	All ?
					Damascus						
−63.1	239.9	−59.9	244.8	−62.9	229.2	−66.4	231.4	−62.9	248.7	0.000	N
−66.4	243.7	−62.9	248.7	−66.4	231.4	−69.9	234.5	−65.8	253.7	0.007	N
−69.6	249.3	−65.8	253.7	−69.9	234.5	−73.4	238.8	−68.6	260.0	0.000	N
−72.6	256.2	−68.6	260.0	−73.4	238.8	−76.7	245.4	−71.0	268.1	0.220	Y
−75.0	265.7	−71.0	268.1	−76.7	245.4	−79.8	256.2	−73.0	278.3	0.276	Y
−77.1	278.5	−73.0	278.3	−79.8	256.2	−82.2	275.0	−74.3	290.7	0.673	Y
−78.4	295.2	−74.3	290.7	−82.2	275.0	−83.2	304.2	−74.8	304.6	0.868	Y
−78.4	314.0	−74.8	304.6	−83.2	304.2	−82.3	333.8	−74.3	318.6	1.000	Y
−77.0	331.1	−74.3	318.6	−82.3	333.8	−79.9	353.1	−73.1	331.1	0.548	Y
−75.0	344.6	−73.1	331.1	−79.9	353.1	−76.9	4.2	−71.1	341.5	0.444	Y
−72.5	354.2	−71.1	341.5	−76.9	4.2	−73.5	10.9	−68.7	349.6	0.046	N
−69.6	0.7	−68.7	349.6	−73.5	10.9	−70.1	15.4	−66.0	356.0	0.000	N
−66.5	6.0	−66.0	356.0	−70.1	15.4	−66.6	18.5	−63.1	1.0	0.000	N
					Baghdad						
−65.6	220.3	−63.1	227.2	−63.6	209.9	−67.2	209.1	−66.7	229.2	0.000	N
−69.2	221.0	−66.7	229.2	−67.2	209.1	−70.9	207.9	−70.2	231.9	0.072	Y
−72.8	222.3	−70.2	231.9	−70.9	207.9	−74.6	206.2	−73.7	235.8	0.139	Y
−76.5	224.9	−73.7	235.8	−74.6	206.2	−78.3	203.3	−77.2	241.8	0.102	Y
−80.2	228.2	−77.2	241.8	−78.3	203.3	−81.9	197.8	−80.4	252.0	0.189	Y
−83.9	236.6	−80.4	252.0	−81.9	197.8	−85.4	183.6	−83.0	271.1	0.289	Y
−87.0	266.7	−83.0	271.1	−85.4	183.6	−87.6	127.3	−84.2	304.1	0.609	Y
−87.0	345.1	−84.2	304.1	−87.6	127.3	−85.6	67.7	−83.1	337.6	0.845	Y
−83.9	14.1	−83.1	337.6	−85.6	67.7	−82.1	52.6	−80.5	357.3	0.662	Y
−80.2	21.5	−80.5	357.3	−82.1	52.6	−78.5	46.9	−77.3	7.9	0.498	Y
−76.5	25.2	−77.3	7.9	−78.5	46.9	−74.8	43.9	−73.9	14.0	0.427	Y
−72.8	27.6	−73.9	14.0	−74.8	43.9	−71.1	42.2	−70.4	18.0	0.000	Y
−69.1	28.7	−70.4	18.0	−71.1	42.2	−67.4	41.0	−66.8	20.7	0.000	N
					Cairo						
−64.9	201.6	−63.6	208.7	−62.0	194.5	−65.4	191.5	−67.2	207.7	0.000	N
−68.4	199.4	−67.2	207.7	−65.4	191.5	−68.7	187.4	−70.8	206.2	0.058	N
−72.0	195.7	−70.8	206.2	−68.7	187.4	−71.9	181.9	−74.5	204.1	0.036	Y
−75.5	190.6	−74.5	204.1	−71.9	181.9	−74.8	174.0	−78.2	200.6	0.354	Y
−78.9	183.2	−78.2	200.6	−74.8	174.0	−77.4	162.6	−81.8	194.1	0.063	Y
−81.9	169.2	−81.8	194.1	−77.4	162.6	−79.3	146.3	−85.1	177.9	0.000	Y
−83.7	142.3	−85.1	177.9	−79.3	146.3	−80.0	125.5	−87.0	126.8	0.129	Y
−83.7	107.5	−87.0	126.8	−80.0	125.5	−79.4	104.6	−85.3	73.5	0.351	Y
−81.8	81.5	−85.3	73.5	−79.4	104.6	−77.5	88.0	−81.9	56.4	0.472	Y
−78.8	66.9	−81.9	56.4	−77.5	88.0	−75.0	76.4	−78.3	49.6	0.535	Y
−75.4	58.9	−78.3	49.6	−75.0	76.4	−72.0	68.4	−74.7	46.0	0.391	N
−72.0	54.0	−74.7	46.0	−72.0	68.4	−68.8	62.8	−71.0	43.9	0.000	N
−68.5	50.7	−71.0	43.9	−68.8	62.8	−65.5	58.7	−67.4	42.4	0.000	N
					Alexandria						
−62.3	185.6	−61.8	193.1	−58.1	179.7	−60.9	175.5	−65.1	189.9	0.000	N
−65.0	180.8	−65.1	189.9	−60.9	175.5	−63.6	170.3	−68.3	185.7	0.000	N
−67.9	175.1	−68.3	185.7	−63.6	170.3	−66.0	164.0	−71.4	179.9	0.011	N
−70.6	167.9	−71.4	179.9	−66.0	164.0	−68.1	156.3	−74.3	172.0	0.350	Y
−72.9	158.4	−74.3	172.0	−68.1	156.3	−69.8	147.1	−76.8	160.6	0.367	Y
−74.8	146.5	−76.8	160.6	−69.8	147.1	−70.8	136.6	−78.6	144.9	0.293	Y
−75.6	132.5	−78.6	144.9	−70.8	136.6	−71.2	125.3	−79.3	125.5	0.282	N
−75.6	117.6	−79.3	125.5	−71.2	125.3	−70.9	113.9	−78.7	106.0	**0.254**	N
−74.7	103.6	−78.7	106.0	−70.9	113.9	−69.8	103.3	−76.9	90.0	**0.170**	N
−73.0	91.4	−76.9	90.0	−69.8	103.3	−68.2	94.1	−74.5	78.5	**0.085**	N
−70.5	82.1	−74.5	78.5	−68.2	94.1	−66.1	86.4	−71.6	70.4	0.000	N
−67.9	74.7	−71.6	70.4	−66.1	86.4	−63.7	80.0	−68.5	64.6	0.000	N
−65.0	69.2	−68.5	64.6	−63.7	80.0	−61.0	74.8	−65.2	60.3	0.000	N

[a]Brightness is normalized to that of the brightest bin. The location of the bins is shown in Figure 3. The rightmost column indicates whether FP3 coverage is complete for each bin. While many bins have incomplete coverage, other CIRS observations indicate that radiated power is low in most of the area that was not mapped by this observation. However, the bold brightness values given for three bins with incomplete rev 61 coverage on Alexandria Sulcus are approximate values based on other FP3 observations, which showed that these regions of Alexandria have nonnegligible brightness.

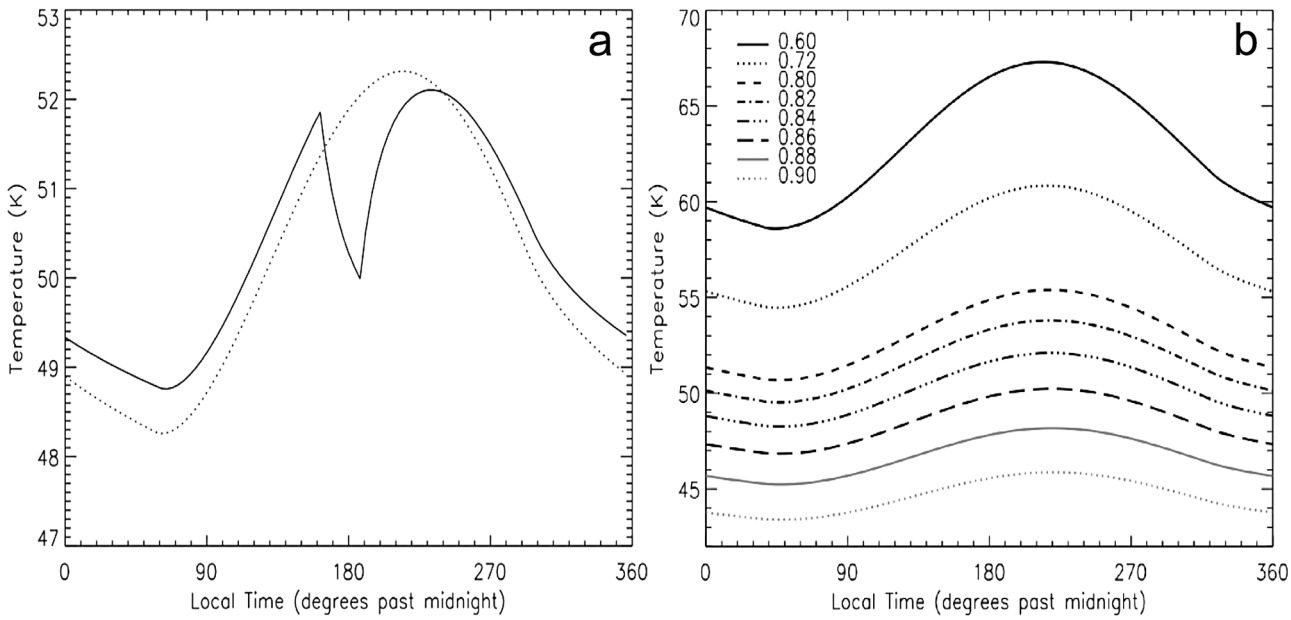

Figure 4. (a) The diurnal surface temperature curve at 80°S, 0°W for rev 91, including the effects of eclipses by Saturn and heating by Saturn radiation (solid line) and with neither (dotted line), assuming "scenario 1" thermophysical properties (Table 3). Temperatures are perturbed during the eclipse, and temperatures at all times of day are also reduced due to the reduction in total diurnal insolation. However, this latter effect is counteracted by Saturn heating: during the observation period, which is near equinox, the effects of eclipses and Saturn heating almost cancel. The total perturbation due to Saturn effects is never more than ~2.0 K. (b) The diurnal surface temperatures during rev 61 at 80°S for the various constant bolometric Bond albedo values indicated and "scenario 1" for the thermal inertia (Table 3), ignoring the effects of Saturn heating and eclipses.

previously discussed, and fitting a blackbody temperature curve to the resulting residual, it is possible to determine how sensitive the calculated endogenic power is to eclipse and Saturn shine effects. The results from these calculations are given in Table 2, which shows that ignoring both the cooling effect of the eclipse and the warming effect of Saturn shine on the surface temperature assuming a uniform thermal inertia profile of 27 MKS results in the endogenic power being underestimated by a mean value of 0.8 GW for rev 61 and 0.1 GW for rev 91. All subsequent endogenic powers are increased for each correction factor and for each rev by the values in Table 2.

2.4. Thermal Inertia Scenarios

[21] Little is known about Enceladus' subsurface structure in the uppermost few meters, although it is likely that its thermal inertia increases with depth due to various compacting mechanisms. The thermal inertia of Enceladus at depths of ~1 cm, as probed by the diurnal thermal wave, has been observed to vary between 9 and 40 MKS between 60°S and 90°N [*Howett et al.*, 2010]. Passive temperatures near the poles are also sensitive to seasonal temperature variations, which are influenced by subsurface thermophysical properties at depths up to ~1 m, and these are less well constrained.

[22] Three different scenarios for thermal inertia profiles have been tested: a constant thermal inertia of 27 MKS at all depths (scenario 1) and two scenarios both of which have a thermal inertia of 27 MKS from the surface to a depth of 1 cm

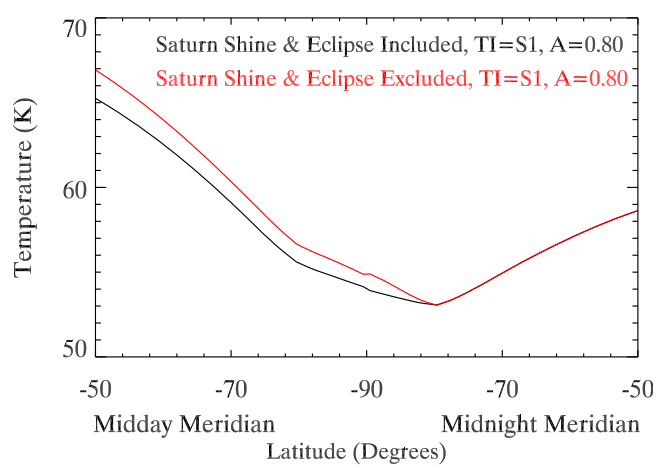

Figure 5. Predicted surface temperatures of Enceladus' southern hemisphere along the midday and midnight meridian at the time of the central stare observation for rev 91 (31 October 2008 at 1807:45 UT) assuming a constant thermal inertia with depth of 27 MKS (referred to in the text as "scenario 1" and shortened in the key to "S1") and bolometric Bond albedo (A) of 0.80. The effect of Saturn shine and eclipse are included in the results shown in black and ignored in those shown in red.

Table 2. Sensitivity of Enceladus' Derived Endogenic Emission to Whether Saturn Shine and Eclipse Events Are Included in the Passive Models for Both Rev 61 and 91[a]

Assumed Conditions for Thermal Model	Endogenic Power for Rev 61 Uniform Spatial Distribution (GW)	Endogenic Power for Rev 61 FP3-Like Spatial Distribution (GW)	Endogenic Power for Rev 61 Central Spatial Distribution (GW)	Endogenic Power for Rev 91 Uniform Spatial Distribution (GW)	Endogenic Power for Rev 91 FP3-Like Spatial Distribution (GW)	Endogenic Power for Rev 91 Central Spatial Distribution (GW)
No eclipse or Saturn shine effects	15.6	13.0	7.7	19.2	16.8	11.8
Eclipse and Saturn shine effects	16.6	13.8	8.2	19.3	16.9	11.9
Difference	1.0	0.9	0.5	0.1	0.1	0.1

[a]The variation is given for both uniform emission along the tiger stripes, nonuniform emission following the spatial variation seen in FP3 (Figure 3), and a model where the central 10% of the field of view is responsible for all emission, for both revs, assuming thermal inertia scenario 1 (Table 3).

but have higher thermal inertias of 100 MKS (scenario 2) and 1000 MKS below 1 cm (scenario 3). A near-surface thermal inertia of 27 MKS was derived for the latitude bin 60°S to 50°S [*Howett et al.*, 2010], this is the closest location to the South polar terrain (SPT) for which thermal inertia has been determined. The lower deep layer thermal inertia value of 100 MKS was selected using results from 2005 Cassini CIRS observations of Enceladus' winter north pole that showed the north polar thermal inertia to be less than 100 MKS to a depth of ~1 m [*Spencer et al.*, 2006]. The higher deep layer thermal inertia value of 1000 MKS was selected to be close to that of solid water ice [*Paige et al.*, 1994]. Figure 6 shows how the predicted surface temperature of Enceladus varies for the midpoint of the rev 91 stare observation for a constant surface bolometric Bond albedo of 0.80 for all three scenarios, ignoring Saturn effects (section 2.3). It shows that during the rev 91 stares the lower subsurface thermal inertia scenarios display slightly higher surface temperatures. As Table 3 shows the scenarios with the higher surface temperatures tend to have lower derived endogenic emissions, as their predicted passive component will be higher. Although this simple trend is complicated by seasonal effects for these observations, as they were obtained close to Saturn's equinox. Table 3 shows that despite the wide range of subsurface thermal inertias considered, for any given assumption for the endogenic emission spatial distribution the effect that changing the assumed thermal inertia has on the calculated endogenic emission is relatively small (<2.4 GW).

[23] Due to the observation times relative to Enceladus' seasonal cycle, the scenarios with high subsurface thermal inertia increase the endogenic emission of the rev 61 observations but decrease that of the rev 91 observations. Scenario 2 is adopted for the subsurface's thermal inertia profile for the remainder of this work, although selecting scenarios 1 or 3 would not significantly change the results, as discussed further in section 2.6.

2.5. Surface Albedo and Its Variation With Incidence Angle

[24] Predicted passive surface temperatures are strongly dependent upon the assumed bolometric Bond albedo A: lower albedos produce higher passive temperatures and thus lower derived endogenic emission. The bolometric Bond albedo of Enceladus has been shown to vary from 0.74 to 0.82 from 70°N to 60°S, with a general trend of increasing albedo toward more southern latitudes [*Howett et al.*, 2010]. ISS images do not show dramatic differences in albedo between the SPT and the rest of Enceladus, except that the tiger stripes themselves are darker than the rest of the SPT especially at near-IR wavelengths [*Porco et al.*, 2006], but a photometric determination of the bolometric albedo of the tiger stripes or the rest of the south polar terrain has yet to be made.

[25] Table 4 shows the effect on the derived heat flow of varying the assumed A from 0.80 (a value consistent with those observed in the southern hemisphere, and used for most other models discussed here) to 0.72 (similar to the minimum observed elsewhere on Enceladus). This albedo reduction would reduce derived heat flows by 3.3–8.0 GW, though heat flows are still significantly higher than the 5.8 ± 1.9 GW previously determined from FP3 data [*Spencer et al.*, 2006], except for the implausible case where all the heat flow is concentrated near the center of the FP1 field of view. Even lower SPT albedos might be considered, but can be shown to be unlikely by comparison of models to passive thermal

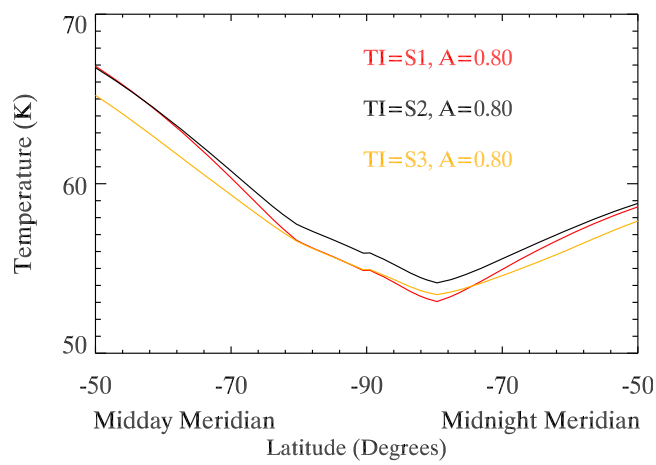

Figure 6. Predicted surface temperatures of Enceladus' southern hemisphere along the midday and midnight meridian at the time of the central stare observation for rev 91 (31 October 2008 at 1807:45 UT) for a constant surface bolometric Bond albedo value of 0.80 but different near-surface thermal properties. Three scenarios outlined in section 2.4 are shown: a constant thermal inertia of 27 MKS with depth (scenario 1, or S1), a constant thermal inertia of 27 MKS above 1 cm depth and 100 MKS below (S2), and a constant thermal inertia of 27 MKS above 1 cm depth and 1000 MKS below (S3). Saturn effects (section 2.3) are not included.

Table 3. Variation in Derived Endogenic Emission Assuming an Albedo of 0.80 and Three Different Subsurface Conditions[a]

Assumed Subsurface Conditions for Thermal Model	Rev 61 Endogenic Power Uniform Spatial Distribution (GW)	Rev 61 Endogenic Power FP3-Like Spatial Distribution (GW)	Rev 61 Endogenic Power Central Spatial Distribution (GW)	Rev 91 Endogenic Power Uniform Spatial Distribution (GW)	Rev 91 Endogenic Power FP3-Like Spatial Distribution (GW)	Rev 91 Endogenic Power Central Spatial Distribution (GW)
Scenario 1	16.6	13.8	8.2	**19.3**	16.9	11.9
Scenario 2	15.5	**12.9**	7.6	17.2	15.0	10.6
Scenario 3	**16.6**	13.8	8.1	16.6	**14.5**	10.2

[a]Scenario 1 assumes a thermal inertia of 27 MKS for the surface and subsurface. Scenarios 2 and 3 both have a thermal inertia of 27 MKS above 1 cm, below this the thermal inertia is assumed to be 100 MKS and 1000 MKS, respectively. The derived endogenic power is given for uniform tiger stripe emission, a nonuniform case that adopts an FP3-like distribution of emission, and a case where the central 10% of the field of view is responsible for all emission, for both revs. Endogenic powers are corrected for Saturn shine and eclipse effects (Table 2) as described in section 2.3. Numbers in boldface are the extreme values for each rev (excluding the unlikely cases where all emission is concentrated in the center of the field of view), which are used to estimate the likely uncertainty range of the heat flow (see section 3).

emission observations taken close to, but not over, the tiger stripe fractures (section 2.6). In section 2.6 we show that $A = 0.80$ fits those observations best, $A = 0.72$ is probably too low, and $A = 0.60$ can be definitively ruled out.

[26] Previous studies have shown that the common assumption that the A is constant with incidence angle i (the angle between the direction of sunlight and the surface normal) can result in overestimation of temperatures near the terminator and the poles, because in reality A tends to increase, reducing temperatures, as i increases [*Squyres and Veverka*, 1982; *Irvine*, 1975]. A method to quantify this $A(i)$ effect has been designed for low-albedo surfaces [*Squyres and Veverka*, 1982]. However, it was later shown that this technique was unsuitable for characterizing the higher-albedo surface of Io [*Simonelli and Veverka*, 1988]. Thus, it is expected that this technique is also unsuitable for characterizing Enceladus' even more reflective surface given that Enceladus has a bolometric Bond albedo of 0.81 between 70°N and 60°S [*Howett et al.*, 2010], compared to a global value of 0.52 for Io [*Simonelli et al.*, 2001].

[27] The bolometric Bond albedo of Triton is 0.65 [*Nelson et al.*, 1990], which is more comparable with that of Enceladus, and Triton's variation in A with i has previously been modeled [*Stansberry et al.*, 1992]. Assuming the same relative variation in albedo with incidence angle for Enceladus, and $A = 0.80$ at zero incidence angle, then during both revs 61 and 91 $A(i)$ will be about 0.89 at the South pole, where the $A(i)$ effect is most pronounced. Figure 4b shows how diurnal surface temperatures at 80°S for rev 61 decrease as A, which is now constant, increases over this range. Thus the lower constant albedo value assumed in our thermophysical model is likely to overestimate Enceladus' high-latitude surface temperatures and hence overestimate the passive thermal background. Since endogenic emission is the residual between the observed CIRS spectra and the passive thermal background, using a constant albedo will result in endogenic emission being underestimated.

[28] Figure 7 shows the effect on surface temperature when the surface bolometric Bond albedo is allowed to vary with incidence angle for two different thermal inertia scenarios: a constant thermal inertia of 27 MKS with depth (scenario 1) and a profile with a thermal inertia of 27 MKS to 1 cm and 100 MKS below (scenario 2). Figure 7 shows that if the albedo is allowed to vary with incidence angle then cooler surface temperatures are produced for both thermal inertia scenarios. Table 4 compares the endogenic emissions calculated for both a constant albedo and one that varies with incidence angle in the same way as Triton for the two emission scenarios. This particular formulation for $A(i)$ would increase derived endogenic heat flow by up to 4.0 GW for both revs 61 and 91. However, it is unlikely that the albedo of Enceladus' south polar terrain varies exactly like that of Triton, with its lower albedo. In fact the ability of our current model, which assumes a constant A of 0.80, to reproduce passive thermal emission near the tiger stripes (section 2.6) suggests that $A(i)$ effects are relatively small. Thus these effects are not included in our preferred heat flow estimates.

2.6. Validation of the Passive Thermal Model by Comparison to High Spatial Resolution Observations

[29] The 1-D passive thermal model can be verified by comparing the passive background spectra predicted by the

Table 4. Variation in Endogenic Power Output for a Constant Albedo of 0.72 and 0.80 and a Triton-Like Dependence of Albedo on Incidence Angle Using an Albedo of 0.80 at Zero Incidence for Revs 61 and 91 Using Scenario 2 for the Subsurface Thermal Inertias[a]

Assumed Conditions for Thermal Model	Rev 61 Endogenic Power Uniform Spatial Distribution (GW)	Rev 61 Endogenic Power FP3-Like Spatial Distribution (GW)	Rev 61 Endogenic Power Central Spatial Distribution (GW)	Rev 91 Endogenic Power Uniform Spatial Distribution (GW)	Rev 91 Endogenic Power FP3-Like Spatial Distribution (GW)	Rev 91 Endogenic Power Central Spatial Distribution (GW)
Constant albedo of 0.80	16.6	13.8	8.2	19.3	16.9	11.9
Constant albedo of 0.72	9.9	8.2	4.9	11.3	9.9	7.0
Varying albedo with incidence angle ($A_0 = 0.80$)	20.9	17.4	10.3	22.5	20.0	13.8

[a]The results have been corrected for Saturn shine and eclipse effects as described in section 2.3. The variation is given for uniform tiger stripe emission, a nonuniform case that adopts an FP3-like distribution of emission, and a case where the central 10% of the field of view is responsible for all emission, for both revs.

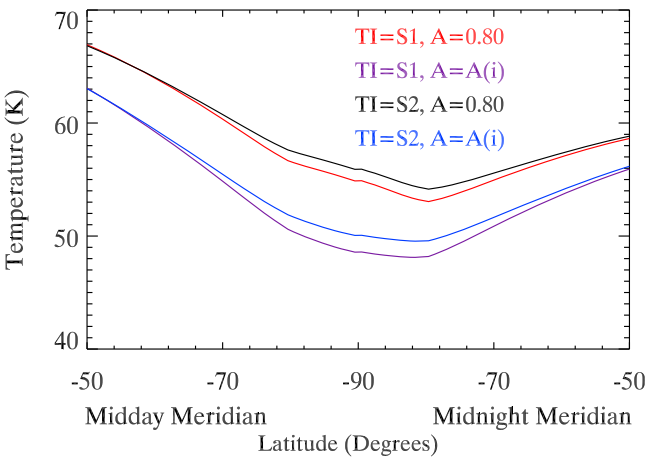

Figure 7. Predicted surface temperatures of Enceladus' southern hemisphere along the midday and midnight meridian at the time of the central stare observation for rev 91 (31 October 2008 at 1807:45 UT) as the surface albedo and thermal properties are varied for thermal inertia scenarios S1 and S2 (section 2.4). Both a constant bolometric Bond albedo (A) value of 0.80 and an albedo that varies with incidence angle ($A(i)$) are shown (see section 2.4 for details). Saturn effects (section 2.3) are not included.

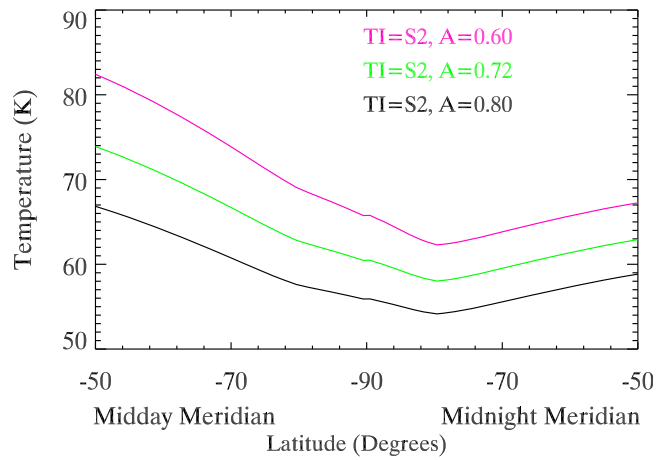

Figure 9. Predicted surface temperatures of Enceladus' southern hemisphere along the midday and midnight meridian at the time of the central stare observation for rev 91 (31 October 2008 at 1807:45 UT) for thermal inertia scenario S2 (section 2.4) as the surface bolometric Bond albedo (A) is varied from 0.60 to 0.72 and 0.80. Saturn effects (section 2.3) are not included.

model to high spatial resolution CIRS observations taken during rev 61, 80 and 91. These observations, the footprints of which are shown in Figure 8, lie within or close to the tiger stripe region but do not include the tiger stripes

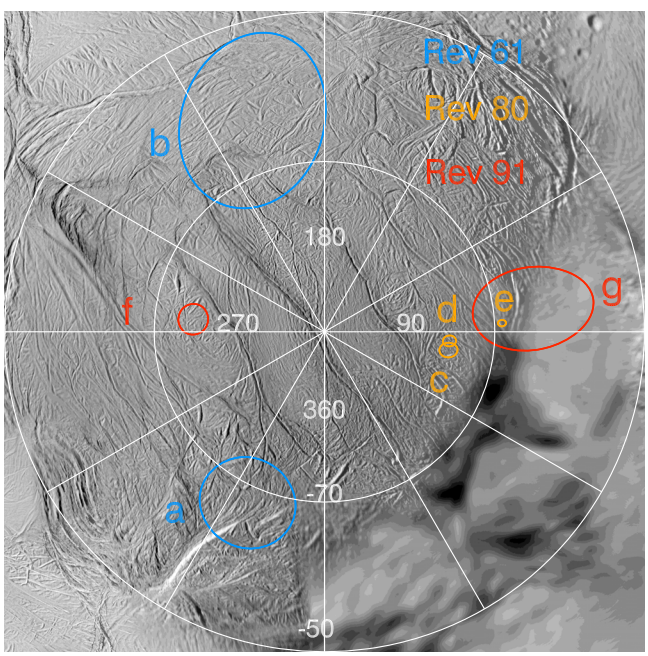

Figure 8. CIRS FP1 footprints for selected high-resolution observations taken during revs 61, 80, and 91. The field of view is approximated by a 3.9 mrad diameter circle. The locations were chosen to lie within the south polar terrain but away from regions of endogenic emission. The blue, orange, and red footprints indicate observations from revs 61, 80, and 91, respectively.

themselves, which are assumed to be the major source of the endogenic heat. Agreement between the model and the observations would suggest that the parameters assumed in the passive model are appropriate for these regions. These same parameters are then likely to be valid for modeling the passive component of the polar stare observations, since the region covered by the polar stares is dominated by terrain with a high albedo similar to that covered by the high spatial resolution observations discussed above. Figure 9 shows the variation in surface temperature with latitude for a models with a bolometric Bond albedo of 0.60, 0.70, and 0.80 for thermal inertia scenario 2. These models are used to calculate the modeled passive thermal background spectra that are compared to CIRS spectra in Figure 10, where the letters in Figure 8 correspond to the plots in Figure 10. Along with these models Figure 10 also shows the predicted radiance for the geometry of each high spatial resolution observations for models that have a varying albedo with incidence angle and have assumed thermal inertia scenarios 1 and 2 and models that use thermal inertia scenarios 1, 2, and 3 with a constant bolometric Bond albedo value of 0.80. The close to zero radiances and lack of spectral features in deep space spectra at times close to the spectra shown in Figure 10 provide an assurance that the spectral calibration is good.

[30] Figure 10 shows that A = 0.72 and 0.60 produce surface temperatures so high they are unable to provide good agreement between the model and the high-resolution CIRS observations, while A = 0.80 produces an excellent fit to the data. This value is therefore assumed in most models when calculating background thermal emission across the entire SPT.

[31] The agreement between the observed emission near the edge of the tiger stripes and the passive background thermal model is the strongest evidence that our thermal model accurately describes passive emission in the tiger strip region, and thus increases confidence in our resulting endogenic emission estimates. In particular the good agree-

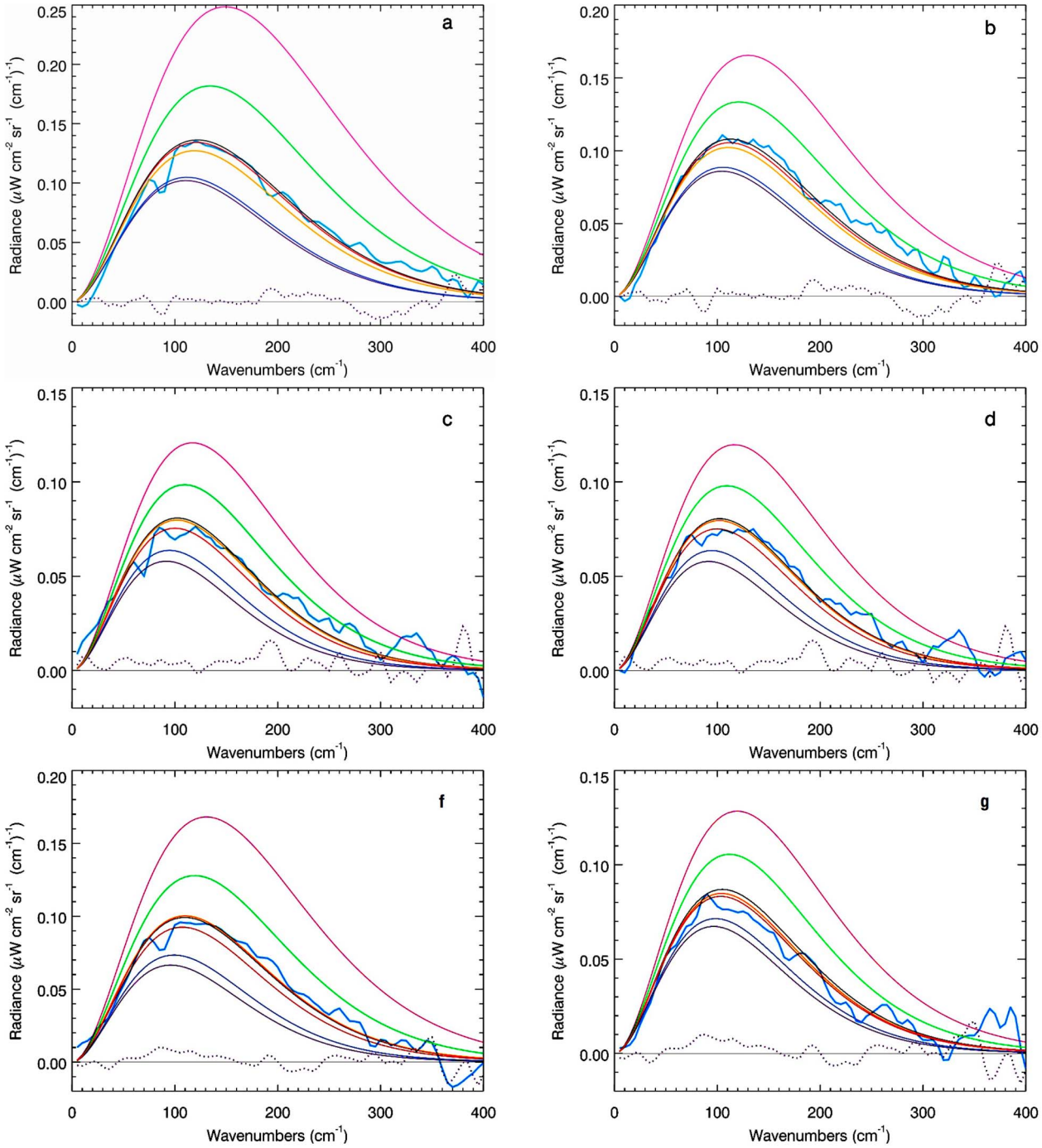

Figure 10. A comparison of the passive thermal model spectra with observed CIRS FP1 spectra for the spectra whose letter in each plot corresponds to the footprints shown Figure 8. None of the models include the effects of Saturn heating or eclipses; CIRS FP1 spectra are shown in light blue. The pink, green, and black lines follow the same color scheme as Figure 9, indicating models that use "scenario 2" for their thermophysical properties (section 2.4) and constant bolometric Bond albedo values of 0.60, 0.72, and 0.80, respectively. The radiance predicted by models using a constant albedo of 0.80 and thermal inertia "scenarios 1, 2, and 3" are also shown, following the same color scheme as Figure 6, shown in red, black, and gold. Finally, Figure 10 also shows the predicted radiance of models that allow the bolometric Bond albedo to vary with incidence angle, following the same color scheme as Figure 7 models with a varying albedo and thermophysical properties. "Scenario 1" and "scenario 2" are given by the solid purple and blue lines. The dotted purple line on each plot indicates the closest deep space spectrum whose near-zero radiance provides a calibration check. All observations from rev 61 were taken in eclipse.

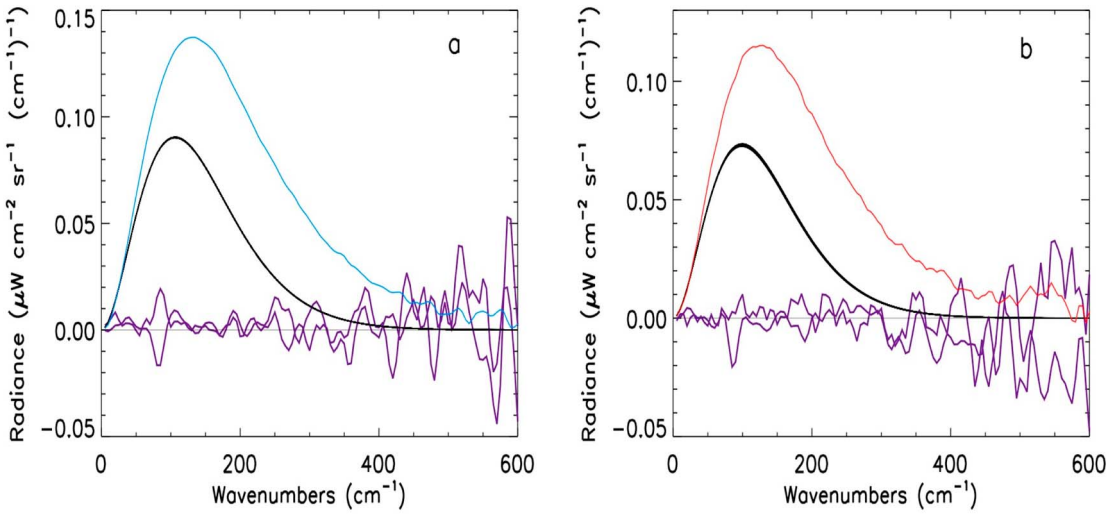

Figure 11. (a and b) Comparison of the modeled passive thermal radiance (black) (determined using thermal inertia scenario 2 (section 2.4) and a constant bolometric Bond albedo of 0.80) to the mean observed FP1 spectra for the rev 61 (blue) and rev 91 (red) south polar stares, respectively. The accuracy of the applied calibration is assured by the lack of spectral features and the near-zero radiance of the deep space spectra taken closest to each of the observations (purple). The difference between the passive thermal radiance and the observed spectra, corrected for the Gaussian spatial response of the FP1 detector and the estimated spatial variations in the tiger stripe emission, gives the spectral signature of the endogenic output.

ment between the model and the CIRS data supports our conclusions that the combined effect of eclipses and Saturn radiation on Enceladus' surface temperature during these observations is small, since without these effects the model agrees well with both rev 61 and 91 data, which were taken during and out of eclipse, respectively.

[32] Not all regions of parameter space have been explored in our thermal models: for instance we do not consider top layer thermal inertias other than the 27 MKS inferred from CIRS observations of midsouthern latitudes on Enceladus. However, as the Figure 10 shows that regardless of the selected thermal inertia scenario models with a constant albedo of 0.80 provide a much closer fit to the CIRS data than the other models tested. Since any successful passive model must reproduce the passive temperatures near the edge of the tiger stripe region, as shown in Figures 8 and 10, successful passive models will also predict similar passive temperatures within the tiger stripe region and thus similar inferred endogenic heat flows. Perverse cases in which thermophysical properties within the tiger stripe region differ significantly from those immediately surrounding the tiger stripes cannot be ruled out, and might produce significantly different inferred heat flows, but we consider such cases to be relatively unlikely. Another possibility that cannot be ruled out is that the observations in Figures 8 and 10 are not purely of passive temperatures, but themselves include an endogenic component. In that case the true endogenic heat flow would be even greater than inferred in this paper.

3. Results

[33] The mean CIRS spectrum of the rev 61 and 91 stares is compared to the predicted passive thermal background, assuming thermal inertia scenario 2 and A = 0.80, in Figures 11a and 11b. The substantial difference between the two radiances indicates a large endogenic component.

[34] This endogenic component for both revs is shown in Figure 12, for both the uniform and nonuniform tiger stripe emission correction and thermal inertia scenario 2, along with their best blackbody fits. For thermal inertia scenario 2 both of the corrected mean residuals of rev 61 are best fitted by a temperature of 99.1 K occupying and area of 2657 km^2 and 2211 km^2 assuming uniform and nonuniform tiger stripe emission, respectively. For rev 91 the mean corrected residuals are fitted by a cooler 92.4 K over 4121 km^2 and 3609 km^2 for uniform and nonuniform tiger stripe emission, respectively. As Table 3 shows, the range of total endogenic emission of Enceladus' south polar terrain determined using the Stefan-Boltzmann law, adjusting for the effect of eclipses and Saturn shine (which are not included in this passive model) for all three thermal inertia scenarios is 12.9 to 16.6 GW for rev 61 and 14.5 to 19.3 GW for rev 91.

[35] We conclude from the above analysis that the uncertainty of the spatial distribution in the emission and uncertainties in Enceladus' subsurface thermophysical properties are the major sources of error in the calculation of the endogenic power (the uncertainties are significantly larger than the statistical error due to observation noise). The maximum and minimum endogenic emission values given in boldface in Table 3, excluding the extreme and unlikely scenario where all emission is concentrated at the center of the FP1 field of view, are used as our estimate of the uncertainty range of the total endogenic emission. We thus estimate that Enceladus' south polar endogenic emission of 14.8 ± 1.9 GW for rev 61 and 16.9 ± 2.4 GW for rev 91, which agree within error and give a combined value of 15.8 ± 3.1 GW. Emission could be several GW lower for lower

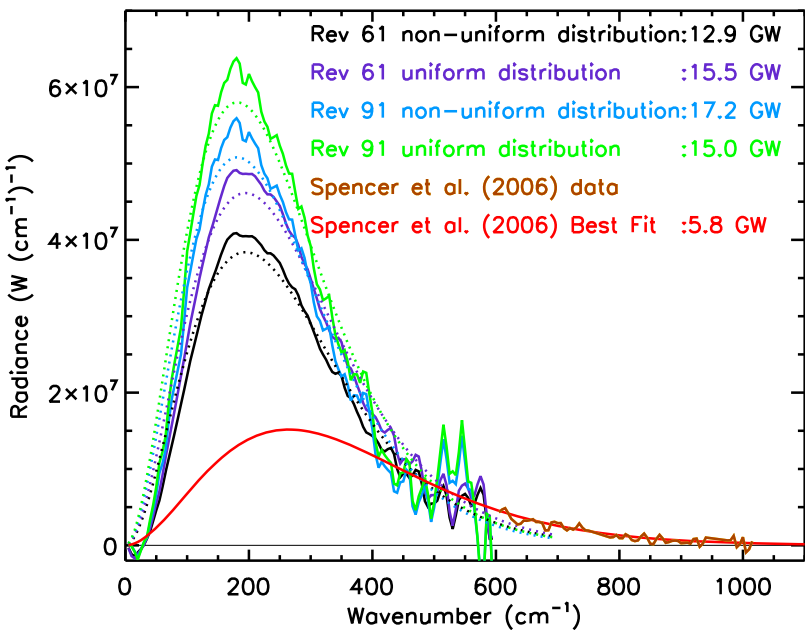

Figure 12. The mean endogenic emission of the FP1 stare observations taken during revs 61 and 91, assuming both uniform and nonuniform emission along the tiger stripes (see section 2.2). The best fitting blackbody temperature fits are given by the dotted lines, which are correspondingly colored. Temperatures of 99.1 K and 92.4 K provide the best fit to rev 61 and 91 for both of the assumed spatial distributions. However, the total surface area of the emission decreases from 2657 km^2 to 2211 km^2 for rev 61 and from 4121 km^2 to 3609 km^2 for rev 91 as the assumed spatial distribution varies from uniform to nonuniform. The 2005 FP3 endogenic emission spectrum used by *Spencer et al.* [2006] to determine the previous lower estimate of endogenic power is also shown, along with the extrapolation of a blackbody fit to that spectrum over the wave number range of the FP1 detector.

albedos than the value of 0.80 assumed in these models, or for highly concentrated spatial distributions of the heat flow, but we consider these scenarios unlikely, as discussed in sections 2.2 and 2.6. It is also possible that the emission is higher than our estimate if it is more spatially extensive than the FP1 fields of view in the rev 61 and rev 91 stare observations, or if south polar albedo is higher than 0.80, for instance due to incidence angle effects as discussed in section 2.5.

[36] If the total length of the tiger stripes is assumed to be 590 km [*Porco et al.*, 2006] and they are assumed to be the sole region of endogenic emission, then the areas of endogenic emission translate to average emission widths of between 3.7 and 7.0 km along the tiger stripes. These are larger than, but comparable to the fracture widths of 2 km derived from ISS images [*Porco et al.*, 2006].

4. Discussion

[37] The total power of the endogenic emission component derived using a simple two-blackbody temperature fit to the rev 61 data, given in section 1.0, is 14.6 GW. This is very close to the 14.5 GW value determined for the same observation before it is corrected for eclipse and Saturn shine effects assuming a uniform distribution in the endogenic emission, a constant albedo of 0.80 and thermal inertia scenario 2. Given this good quality fit it is interesting that the same technique for rev 91 yields very different results: the simple model predicts an endogenic emission of 24.8 GW, compared to the more complex model's uncorrected value of 17.0 GW for the same assumptions as the rev 61 analysis. The reason for this difference may lie in the inability of the simple two-temperature blackbody fit to the data to account for ranges in passive surface temperatures, which arise from seasonal and diurnal solar insolation variations. This effect is most pronounced in the rev 91 observations, since they cover a larger area and more latitudes than the rev 61 observations.

[38] Figure 12 compares the endogenic spectra calculated here to the FP3 endogenic emission spectrum used to derive the previous lower endogenic power estimate [*Spencer et al.*, 2006]. The best fit blackbody curves to the endogenic spectra derived in that paper are shown in red, extrapolated over the full FP1 and FP3 wave number range. Figure 12 shows that the endogenic component of the 2008 FP1 stare observations and the 2005 FP3 data previously used to determine Enceladus' heat flow show consistent fluxes at 600 cm^{-1} where the data sets overlap. Figure 12 shows how at lower wave numbers the FP1 endogenic emission exceeds that extrapolated from the FP3 single-temperature spectral fit, regardless of the emission distribution assumed. As previously speculated the difference between the FP3 spectral fit and the endogenic component of the FP1 spectrum is likely due to low-temperature endogenic emission that the FP3 detector is insensitive to. Similarly, the extrapolated fits to the FP1 data fall below the 2005 FP3 data, because the endogenic radiation detected by FP3 is emitted at a higher temperature. However, Figure 12 shows that the contribution of this

additional high-temperature emission to the total power, which is given by the area under the curves, is negligible.

[39] A variation with wave number in the optical properties of water ice may explain why the emission falls below the best blackbody fit at low wave numbers, as shown in Figure 12. Mie calculations have shown this to be the likely explanation for similar decreases in brightness temperature with decreasing wave numbers in the Cassini/CIRS spectrum of Saturn's A, B, and C rings below 50 cm^{-1} [*Spilker et al.*, 2006].

[40] Note that our new estimate of Enceladus' total endogenic power does not include the power lost by latent heat of water vapor of the plume, estimated to be about 0.7 GW [*Ingersoll and Pankine*, 2010], or potential endogenic thermal power radiated from regions away from the south pole, including any heat radiated over wide areas at low temperature which would be impossible to distinguish from passive surface heating by sunlight. The total endogenic power generated by Enceladus may thus be higher still.

5. Conclusion

[41] The endogenic power derived here is substantially higher than the previous estimate based on >600 cm^{-1} data, but it is also more reliable since it derives from observations at wave numbers where the bulk of the power is radiated (Figure 12). Explaining this high heat flow using current orbital evolution models is difficult because over large time scales those models predict equilibrium heating rates an order of magnitude lower than those observed [*Meyer and Wisdom*, 2007]. Although recent work indicates that higher endogenic powers could be sustainable if Saturn's Q value lower than its current value, which was determined by limits on the change of Mimas' semimajor axis over 4.6 Gy [*Lainey et al.*, 2010; *Meyer and Wisdom*, 2010]. Another possibility is that Enceladus current orbital state is stable and tidal energy is stored inside Enceladus over long time periods. It is then released periodically by bursts of intense activity, such as that currently observed. Another possibility is that the orbital/tidal equilibrium of Enceladus is unstable and that its current high activity is due to recent changes in its orbital eccentricity. Such variability appears to be consistent with both the episodic resurfacing of Enceladus observed in ISS images [*Helfenstein*, 2010] and the unsustainably high loss rates of ^{40}Ar observed in the Enceladus plume [*Waite et al.*, 2009]. Decoupling of the ice shell by a subsurface water layer was required to reproduce the previous conservative endogenic heat flow estimate [*Nimmo et al.*, 2007], the new higher heat flow estimates make liquid water even more likely, enhancing the interest of Enceladus as an astrobiological target.

[42] **Acknowledgments.** Thanks are due to the Cassini project and especially the CIRS team that made these data possible. This work was supported by the Cassini project and NASA grants NNG06GF41G and NNX07AU40G.

References

Abramov, O., and J. Spencer (2009), Endogenic heat from Enceladus' south polar fractures: New observations, and models of conductive surface heating, *Icarus*, *199*, 189–196, doi:10.1016/j.icarus.2008.07.016.

Brown, R. H., et al. (2006), Composition and physical properties of Enceladus' surface, *Science*, *311*, 1425–1428, doi:10.1126/science.1121031.

Collins, G., and J. Goodman (2007), Enceladus's south polar sea, *Icarus*, *189*, 72–82, doi:10.1016/j.icarus.2007.01.010.

Flasar, F. M., et al. (2004), Exploring the Saturn system in the thermal infrared: The composite infrared spectrometer, *Space Sci. rev.*, *115*, 169–297, doi:10.1007/s11214-004-1454-9.

Hanel, R. A., B. J. Conrath, V. G. Kunde, J. C. Pearl, and J. A. Pirraglia (1983), Albedo, internal heat flux, and energy balance of Saturn, *Icarus*, *53*, 262–285, doi:10.1016/0019-1035(83)90147-1.

Hansen, C. J., L. Esposito, A. I. F. Stewart, J. Colwell, A. Hendrix, W. Pryor, D. Shemansky, and R. West (2006), Enceladus' water vapor plume, *Science*, *311*, 1422–1425, doi:10.1126/science.1121254.

Helfenstein, P. (2010), Planetary science: Tectonic overturn on Enceladus, *Nat. Geosci.*, *3*(2), 75–76, doi:10.1038/ngeo763.

Howett, C. J. A., J. R. Spencer, J. Pearl, and M. Segura (2010), Thermal inertia and bolometric Bond albedo values for Mimas, Enceladus, Tethys, Dione, Rhea and Iapetus as derived from Cassini/CIRS measurements, *Icarus*, *206*, 573–593, doi:10.1016/j.icarus.2009.07.016.

Ingersoll, A. P., and A. A. Pankine (2010), Subsurface heat transfer on Enceladus: Conditions under which melting occurs, *Icarus*, *206*, 594–607, doi:10.1016/j.icarus.2009.09.015.

Irvine, W. (1975), Multiple scattering in planetary atmospheres, *Icarus*, *25*, 175–204, doi:10.1016/0019-1035(75)90019-6.

Lainey, V., O. Karatekin, J. Desmars, and S. Charnoz (2010), Saturnian tidal dissipation from astromteric observations, *Bull. Am. Astron. Soc.*, *41*, 936.

Meyer, J., and J. Wisdom (2007), Tidal heating in Enceladus, *Icarus*, *188*, 535–539, doi:10.1016/j.icarus.2007.03.001.

Meyer, J., and J. Wisdom (2010), Tidal heating and orbital evolution of Enceladus, paper presented at European Geophysical Union meeting, Vienna, Abstract EGU2010–3672.

Nelson, R. M., B. J. Buratti, B. D. Wallis, W. D. Smythe, L. J. Horn, A. L. Lane, M. J. Mayo, and K. E. Simmons (1990), Spectral geometric albedo and bolometric Bond albedo of Neptune's satellite Triton from Voyager observations, *Geophys. Res. Lett.*, *17*, 1761–1764, doi:10.1029/GL017i010p01761.

Nimmo, F., J. R. Spencer, R. T. Pappalardo, and M. E. Mullen (2007), Shear heating as the origin of the plumes and heat flux on Enceladus, *Nature*, *447*, 289–291, doi:10.1038/nature05783.

Paige, D., J. Bachman, and K. Keegan (1994), Thermal and albedo mapping of the polar regions of Mars using Viking thermal mapper observations: 1. North polar region, *J. Geophys. Res.*, *99*(E12), 25,959–25,991, doi:10.1029/93JE03428.

Porco, C. C., et al. (2006), Cassini observes the active south pole of Enceladus, *Science*, *311*, 1393–1401, doi:10.1126/science.1123013.

Postberg, F., S. Kempf, J. Schmidt, N. Brilliantov, A. Beinsen, B. Abel, U. Buck, and R. Srama (2009), Sodium salts in E ring ice grains from an ocean below the surface of Enceladus, *Nature*, *459*, 1098–1101, doi:10.1038/nature08046.

Roberts, J., and F. Nimmo (2008), Tidal heating and the long-term stability of a subsurface ocean on Enceladus, *Icarus*, *194*, 675–689, doi:10.1016/j.icarus.2007.11.010.

Ross, M., and G. Schubert (1989), Viscoelastic models of tidal heating in Enceladus, *Icarus*, *78*, 90–101, doi:10.1016/0019-1035(89)90071-7.

Schubert, G., J. D. Anderson, B. J. Travis, and J. Palguta (2007), Enceladus: Present internal structure and differentiation by early and long-term radiogenic heating, *Icarus*, *188*, 345–355, doi:10.1016/j.icarus.2006.12.012.

Simonelli, D., and J. Veverka (1988), Bolometric albedos and diurnal temperatures of the brightest regions on Io, *Icarus*, *74*, 240–261, doi:10.1016/0019-1035(88)90040-1.

Simonelli, D., C. Dodd, and J. Veverka (2001), Regolith variations on Io: Implications for bolometric albedos, *J. Geophys. Res.*, *106*, 33,241–33,252, doi:10.1029/2000JE001350.

Smith, M. D. (2002), CIRS field-of-view test of May 10 and 11 2002, *Tech. Rep.*, NASA, Greenbelt, Md.

Spahn, F. (2006), Cassini dust measurements at Enceladus and implications for the origin of the E ring, *Science*, *311*, 1416–1418, doi:10.1126/science.1121375.

Spencer, J. R., L. A. Lebofsky, and M. V. Sykes (1989), Systematic biases in radiometric diameter determinations, *Icarus*, *78*, 337–354, doi:10.1016/0019-1035(89)90182-6.

Spencer, J. R., J. C. Pearl, M. Segura, F. M. Flasar, A. Mamoutkine, P. Romani, B. Buratti, A. Hendrix, L. J. Spilker, and R. M. C. Lopes (2006), Cassini encounters Enceladus: Background and the discovery of a south polar hot spot, *Science*, *311*, 1401–1405, doi:10.1126/science.1121661.

Spilker, L. J., S. H. Pilorz, S. G. Edgington, B. D. Wallis, S. M. Brooks, J. C. Pearl, and F. M. Flasar (2006), Cassini CIRS observations of a roll-off in Saturn ring spectra at submillimeter wavelengths, *Earth Moon Planets*, *96*, 149–163, doi:10.1007/s11038-005-9060-8.

Spitale, J., and C. Porco (2007), Association of the jets of Enceladus with the warmest regions on its south polar fractures, *Nature*, *449*, 695–697, doi:10.1038/nature06217.

Squyres, S., and J. Veverka (1982), Variation of albedo with solar incidence angle on planetary surfaces, *Icarus*, *50*, 115–122, doi:10.1016/0019-1035(82)90103-8.

Stansberry, J., R. V. Yelle, J. I. Lunine, and A. S. McEwen (1992), Triton's surface-atmosphere energy balance, *Icarus*, *99*, 242–260, doi:10.1016/0019-1035(92)90144-V.

Tobie, G., O. Cadek, and C. Sotin (2008), Solid tidal friction above a liquid water reservoir as the origin of the south pole hotspot on Enceladus, *Icarus*, *196*, 642–652, doi:10.1016/j.icarus.2008.03.008.

Waite, J. H., Jr., et al. (2009), Liquid water on Enceladus from observations of ammonia and ^{40}Ar in the plume, *Nature*, *460*, 487–490, doi:10.1038/nature08153.

Yoder, C. F. (1979), How tidal heating in Io drives the galilean orbital resonance locks, *Nature*, *279*, 767–770, doi:10.1038/279767a0.

C. J. A. Howett and J. R. Spencer, Southwest Research Institute, 1050 Walnut St., Ste. 300, Boulder, CO 80302, USA. (howett@boulder.swri.edu)

J. Pearl and M. Segura, NASA Goddard Space Flight Center, Greenbelt, MD 20771, USA.